Electron momentum density in disordered muffin-tin $Cu_{1-x}Ni_x$ in the average-t-matrix approximation

P. E. Mijnarends
Netherlands Energy Research Foundation (ECN), 1755 ZG Petten (N.H.), The Netherlands

A. Bansil
Physics Department, Northeastern University, Boston, Massachusetts 02115

(Received 3 November 1978)

In an earlier article we discussed the formalism for evaluating the average electron-momentum density in a random binary alloy by using the average-t-matrix approximation to treat the disorder and muffin-tin potentials to represent the constituent atoms. The present paper considers the application of this formalism to $Cu_{1-x}Ni_x$ over a range of alloy compositions. The characteristic effects of disorder on the spectral momentum density $<\rho(\vec{p}, E)>$ are delineated. In discussing the momentum density $<\rho(\vec{p})>$ we focus on how this quantity changes as x increases from 0 to 1 and the Ni d band develops from a virtual bound state below the Fermi energy into a transition-metal d band interacting the Fermi energy. Our detailed predictions in this regard should be amenable to experimental verification by two-dimensional positron-annihilation experiments.

I. INTRODUCTION

Recent theoretical work on the electronic structure of disordered metals has focused largely on the properties of the muffin-tin model.[1,2] The motivation for this stems from the fact that the one- and two-band tight-binding model Hamiltonians are too simple to represent the currently available experimental information concerning the electronic spectrum of transition- and noble-metal alloys. In this connection, two of the most commonly used approximation schemes have been the average-t-matrix (ATA) and coherent-potential (CPA) approximations. Both belong to the class of the so-called single-site approximations. However, of the two, only the CPA treats the disorder self-consistently, and is to be preferred. The attractiveness of the ATA stems mainly from its simplicity in application to realistic models.

We emphasize that the calculation of the momentum density $\langle\rho(\vec{p})\rangle$ in a disordered alloy entails a significantly greater effort than calculation of the more familiar average electronic density of states $\langle\rho(E)\rangle$. Even in a perfect crystal, to compute the momentum density a knowledge of both the electronic energy levels and the corresponding Bloch wave functions is required. By contrast, the electronic density of states is determined completely in terms of the Bloch energy levels alone. This physical difference manifests itself in the fact that in order to evaluate $\langle\rho(\vec{p})\rangle$, in addition to the on-the-energy-shell matrix elements, the detailed momentum dependence of the off-the-energy-shell matrix elements of the atomic scattering operators of the constituent atoms is required.[3] The $\langle\rho(E)\rangle$ calculation, on the other hand, proceeds in terms of only the on-the-energy-shell elements. Indeed, although detailed studies of the electronic densities of states in a variety of transition- and noble-metal alloys have been carried out using the ATA,[4-7] and more recently the muffin-tin CPA,[8-10] no corresponding calculation of the momentum density exists at the present time. Some momentum-density work within the framework of the one-band tight-binding model Hamiltonian has, however, appeared recently.[11,12]

In briefly summarizing some of the relevant experimental techniques, we note that for dilute alloys the concentration dependence of specific Fermi-surface radii and the damping of the corresponding electronic states is measurable via de-Haas–van Alpen experiments.[13,14] The changes in the energies of some of the transitions as a function of alloy composition have been monitored via optical-reflectivity measurements.[15] Photoemission experiments, especially in their current angularly resolved form, measure the bulk electronic density of states, provided surface and matrix-element effects are neglected.[16,17] Under similar simplifying assumptions, soft-x-ray emission allows the determination of the component charge densities associated with the constituent atoms in an alloy.[18] The densities of states at the Fermi energy are obtainable from specific-heat and magnetic-susceptibility measurements.

Of particular interest to us here are the Compton scattering[19] and positron annihilation techniques[20-22] which measure the momentum density in a crystal. Since these experiments do not require long electronic mean free paths, they have the advantage of being applicable to concentrated alloys. Both techniques serve not only to determine Fermi-surface radii, but also to provide detailed information about the electronic wave functions that is not

available from most of the other current experiments on disordered alloys. In comparing the two techniques it is noteworthy that positron spatial distribution effects complicate the interpretation of the experimental positron annihilation profiles.[23] By contrast, Compton profiles do not involve these difficulties of interpretation, but suffer instead from problems of resolution: the usual experimental measurement implies an integration over two of the three momentum components and, in addition, the resolution attainable in γ-ray Compton scattering is at least an order of magnitude lower than for positron annihilation in metals. In this regard, the positron annihilation experiments especially offer attractive possibilities due to the high resolution possible in two-dimensional angular correlation machines.[21,24,25] Spin-polarized measurements in magnetic materials are also possible via this technique.[26-28]

In an earlier article the ATA formalism for the momentum density in disordered muffin-tin alloys was discussed.[3] In considering the application of this formalism to $Cu_{1-x}Ni_x$, the present paper emphasizes the characteristic effects of disorder on the electron momentum density in an alloy. Our detailed predictions with regard to the momentum density in $Cu_{1-x}Ni_x$ should be amenable to experimental verification by high-resolution two-dimensional angular correlation experiments. The problem of extending the muffin-tin CPA to obtain momentum densities, and that of including the effects of the positron spatial distribution in these calculations, will be taken up elsewhere.

An outline of the present paper follows. To make the discussion self-contained, some of the relevant formulas are outlined in Sec. II. The numerical considerations involved in handling the off-the-energy-shell matrix elements of the $A(B)$ scattering matrix $t_{A(B)}(p,\sqrt{E})$ for $p \neq \sqrt{E}$ are delineated. In our presentation of the results of our calculations in Sec. III, the spectral momentum density $\langle\rho(\vec{p},E)\rangle$ is considered as a function of E for a range of alloy compositions. The integrated momentum density $\langle\rho(\vec{p})\rangle$ in $Cu_{0.75}Ni_{0.25}$, with $\vec{p}$ along the $\langle 110\rangle$ direction, is compared with the corresponding calculations for Cu and Ni crystals. As the Ni concentration is increased, the Fermi energy in alloy eventually drops below the top of the Ni d band, and hole ellipsoids develop around the point X in the Brillouin zone. Owing to symmetry constraints, the appearance of X-hole ellipsoids does not cause a break in the momentum density around the point X. Nevertheless, we show that these hole pockets can be observed as dips in $\langle\rho(\vec{p})\rangle$ at higher momenta along appropriately chosen directions in momentum space.

II. THEORY

The configurationally averaged electron momentum density in the disordered alloy $A_{1-x}B_x$ is given by

$$\langle\rho(\vec{p})\rangle = \int_{-\infty}^{E_F} dE \langle\rho(\vec{p},E)\rangle \tag{2.1}$$

as an integral of the spectral momentum density $\langle\rho(\vec{p},E)\rangle$ up to the Fermi energy E_F. As discussed in Ref. 3, for the ATA applied to the muffin-tin Hamiltonian

$$\langle\rho(\vec{p},E)\rangle = -\frac{1}{\pi}\mathrm{Im}\Big\{(E+i0^+-p^2)^{-1}+(4\pi)^2N(E+i0^+-p^2)^{-2}\sum_{LL'}Y_L(\hat{p})\Big[\Big(\langle t_l(p,p)\rangle-\frac{\langle t_l(p,\kappa)\rangle\langle t_l(\kappa,p)\rangle}{\langle t_l(\kappa,\kappa)\rangle}\Big)\delta_{LL'} + \frac{\langle t_l(p,\kappa)\rangle}{\langle t_l(\kappa,\kappa)\rangle}[\langle t(\kappa,\kappa)\rangle^{-1}-B(\vec{k},E)]^{-1}_{LL'}\frac{\langle t_{l'}(\kappa,p)\rangle}{\langle t_{l'}(\kappa,\kappa)\rangle}\Big]Y_{L'}(\hat{p})\Big\}. \tag{2.2}$$

Here $\kappa \equiv \sqrt{E}$, $L \equiv (l,m)$ is a composite index which includes both the orbital and magnetic quantum numbers, and $\vec{k}$ is the reduced wave vector corresponding to the momentum $\vec{p}$. The Lth spherical harmonic associated with the unit vector $\hat{x}$ is denoted by $Y_L(\hat{x})$, and $B(\vec{k},E)$ is the matrix of the usual KKR structure functions. The quantities $\langle t(p,q)\rangle$ are the momentum matrix elements of the average t matrix

$$\langle t\rangle = (1-x)t_A + xt_B, \tag{2.3}$$

and are related to the corresponding matrix elements of the A and B scattering operators $t_A(p,q)$ and $t_B(p,q)$ (t_A, t_B, and $\langle t\rangle$ are diagonal matrices in angular momentum space). The on-the-energy-shell matrix elements $t_{A(B)}(\kappa,\kappa)$ are given in terms of the customary scattering phase shifts $\delta_l^{A(B)}(E)$:

$$t_l^{A(B)}(\kappa,\kappa) = -\kappa^{-1}\sin\delta_l^{A(B)}\exp(i\delta_l^{A(B)}). \tag{2.4}$$

In contrast, the evaluation of the off-the-energy-shell matrix elements $t_{A(B)}(p,\kappa)$ and $t_{A(B)}(p,p)$ for $p \neq \kappa$ is more involved. The relevant equations discussed in Ref. 3 for $E>0$ are

$$t_l^{A(B)}(p,\kappa) = t_l^{A(B)}(\kappa,p) = s_l^{A(B)}(p,E)\cot\delta_l^{A(B)} t_l^{A(B)}(\kappa,\kappa), \tag{2.5}$$

$$\mathrm{Im}\, t_l^{A(B)}(p,p) = [s_l^{A(B)}(p,E)]^2 \cot\delta_l^{A(B)} \times \mathrm{Re}\, t_l^{A(B)}(\kappa,\kappa). \tag{2.6}$$

Here

$$s_l^{A(B)}(p,E) = -\kappa\int_0^{R_m} dr\, r^2 j_l(pr) \times V^{A(B)}(r) R_l^{A(B)}(r,E) \tag{2.7}$$

is given by an integral involving the regular solution $R_l^{A(B)}(r,E)$ of the radial Schrödinger equation for the muffin-tin potential $V^{A(B)}(r)$. In Eq. (2.7), R_m denotes the radius of the muffin-tin sphere and j_l the lth spherical Bessel function.

Equations (2.5)–(2.7) show that the p dependence of $t_l^{A(B)}(p,\kappa)$ and $\mathrm{Im}\, t_l^{A(B)}(p,p)$ arises through the quantity $s_l^{A(B)}(p,E)$. If $p \to \kappa$, $t_l^{A(B)}(p,\kappa)$ must reduce to $t_l^{A(B)}(\kappa,\kappa)$, which in view of Eq. (2.5) implies the equality

$$s_l^{A(B)}(\kappa,E) = \tan\delta_l^{A(B)}(E). \tag{2.8}$$

The limiting behavior (2.8) for the quantities $s_l^{A(B)}(p,E)$ can be displayed explicitly by rewriting Eq. (2.7) as

$$s_l^{A(B)}(p,E) = -\kappa R_m^2[j_l(pR_m), R_l^{A(B)}(R_m,E)] - \kappa(E-p^2)\int_0^{R_m} dr\, r^2 j_l(pr) R_l(r,E). \tag{2.9}$$

Here, $[j_l, R_l]$ denotes the Wronskian of j_l and R_l. [The derivation of Eq. (2.9) is outlined in Appendix B.] In Eq. (2.9), for $p^2 = E$, the second term does not contribute, and the validity of relation (2.8) then follows by recalling the Wronskian identity $[j_l(\kappa r), n_l(\kappa r)] = -1/\kappa r^2$ and the fact that the normalization of the wave function $R_l^{A(B)}(r,E)$ in Eqs. (2.7) and (2.9) is implicitly given by $R_l^{A(B)}(R_m,E) = j_l(\kappa R_m) - \tan\delta_l^{A(B)} n_l(\kappa R_m)$, where n_l denotes the lth spherical Neumann function. We note in passing that Eq. (2.9) applies for $E>0$ as well as for $E<0$.

It is noteworthy that the on-the-energy-shell matrix elements $t_l^{A(B)}(\kappa,\kappa)$ are usually computed via the logarithmic derivatives of the $A(B)$ radial wave functions $R_l^{A(B)}(R_m,E)$, which amounts to using only the first term in Eq. (2.9) for $p=\kappa$. For this reason, the form (2.9) has a practical advantage over (2.7), as it is guaranteed to yield the proper limiting behavior (2.8), which, as discussed below, is essential for the cancellation of the free-electron poles in Eq. (2.2) for $\langle\rho(\vec{\mathfrak{p}},E)\rangle$. In addition, Eq. (2.9), in contrast to (2.7), does not involve the potential $V^{A(B)}(r)$ in the integrand and, therefore, allows the evaluation of the off-the-energy-shell matrix elements corresponding to shifts in the muffin-tin zeros of the A and B atomic potentials more conveniently. Such constant shifts are necessary within the framework of semiempirical models including charge transfer in transition- and noble-metal alloys.[4,2] Finally, we note that the integral in the second term in Eq. (2.9) varies sufficiently smoothly that its computation for a general p and E can be carried out efficiently via numerical interpolation in a table of values of this integral over a suitable mesh in p and E space.

In perfect crystals it is well known that the symmetry of the lattice can force the contributions of many energy bands to vanish in specific regions of momentum space. Reference 29 discusses the details of this selection rule, and presents tables showing which energy bands give nonzero contributions at various momenta $\vec{\mathfrak{p}}$ in the cubic lattices. We emphasize that the results of Ref. 29 are directly applicable to the present case because the average Green's function, and hence the spectral momentum density, in a disordered alloy posesses the symmetry of the point periodic lattice. Thus, in the first Brillouin zone (i.e., for $\vec{\mathfrak{p}} = \vec{k}$), only the bands belonging to the totally symmetric representation (e.g., Δ_1, Σ_1, and Λ_1) will give a nonvanishing contribution to $\langle\rho(\vec{\mathfrak{p}},E)\rangle$. This consideration will be found useful in the following discussion.

III. RESULTS

To understand the nature of the momentum density in an alloy, we consider first the spectral momentum density $\langle\rho(\vec{\mathfrak{p}},E)\rangle$.

The apparent free-electron poles in expression (2.2) do not lead to singular behavior of $\langle\rho(\vec{\mathfrak{p}},E)\rangle$ in the vicinity of $E=p^2$. [The proof of this statement uses, among other things, the fact that $\langle t_l(p,\kappa)\rangle / \langle t_l(\kappa,\kappa)\rangle \to 1$ for $p \to \kappa$ and, as noted above,

implies that care be taken in the numerical computation of $\langle t_l(p,\kappa)\rangle$.[3] In the perfect-crystal limit, the term in large parentheses in (2.2) (the term proportional to $\delta_{LL'}$) can be shown to give a vanishing contribution. Our experience with $Cu_{1-x}Ni_x$ suggests that this term may generally be expected to yield only a small smooth contribution even in the alloy. The structure in $\langle\rho(\vec{p},E)\rangle$ therefore arises primarily through the inverse matrix $[\langle t(\kappa,\kappa)\rangle^{-1}-B(\vec{k},E)]^{-1}$, or equivalently via the complex energy zeros of the secular equation[5,10]

$$\|\langle t(\kappa,\kappa)\rangle^{-1}-B(\vec{k},E)\|=0. \tag{3.1}$$

For a perfect $A(B)$ crystal $\langle t(\kappa,\kappa)\rangle\to t_{A(B)}(\kappa,\kappa)$, and Eq. (3.1) reduces to the familiar KKR equation and yields the usual Bloch energy bands. In a disordered alloy these energy bands become complex, the imaginary parts of the energy representing the damping of perfect Bloch states due to disorder. Such complex energy bands have been obtained in the ATA[2] and the CPA[10] for a variety of transition- and noble-metal alloys, and have been useful in discussing many aspects of their electronic spectrum.

Equation (2.2) shows that, for a given reduced wave vector $\vec{k}$, the contributions to $\langle\rho(\vec{p},E)\rangle$ will be nonzero only for $\vec{p}=\vec{k}+\vec{K}_n$, where $\vec{K}_n$ is a vector of the reciprocal lattice.[30] As noted above, at points of high symmetry contributions of certain energy bands to $\langle\rho(\vec{p},E)\rangle$ can be suppressed in specific regions of momentum space owing to the symmetry of the average alloy.[31] For this reason, in illustrating the behavior of $\langle\rho(\vec{p},E)\rangle$ in Fig. 1 we have chosen $\vec{k}=\vec{k}_0\equiv(0.166, 0.415, 0.664)2\pi/a$, which is a general point in the Brillouin zone. Figure 1 shows that the normal contribution to $\langle\rho(\vec{p},E)\rangle$ as well as the Umklapp contribution corresponding to the (1, 1, 1) reciprocal-lattice vector as a function of E consists of peaks of finite width. The energy location of these peaks is seen to be well correlated with the real parts of the complex energy solutions of Eq. (3.1) for $\vec{k}=\vec{k}_0$, which are marked along the horizontal axis in Fig. 1.

A complex energy level in an alloy that possesses a large imaginary part may not lead to a distinct peak in the spectral function. Thus, for example, in Fig. 1(a) for $Cu_{0.75}Ni_{0.25}$ (i.e., $x=0.25$), in the energy regime of the Ni resonance, several closely spaced complex levels with imaginary parts comparable to their spacing are seen to give just one broad peak around 0.55 Ry. We emphasize that the real and imaginary parts of a complex energy level in the alloy determine only the position and width of the corresponding spectral peak, and contain no information about its weight. The only general statement that can be made with regard to the weights is that if an energy level remains unsplit on alloying (for example, levels such as $X_{4'}$, $L_{2'}$, and Γ_1 in $Cu_{1-x}Ni_x$), then its total spectral weight, i.e., the quantity $\sum_n\rho(\vec{k}+\vec{K}_n,E)$, remains approximately equal to unity, as in the

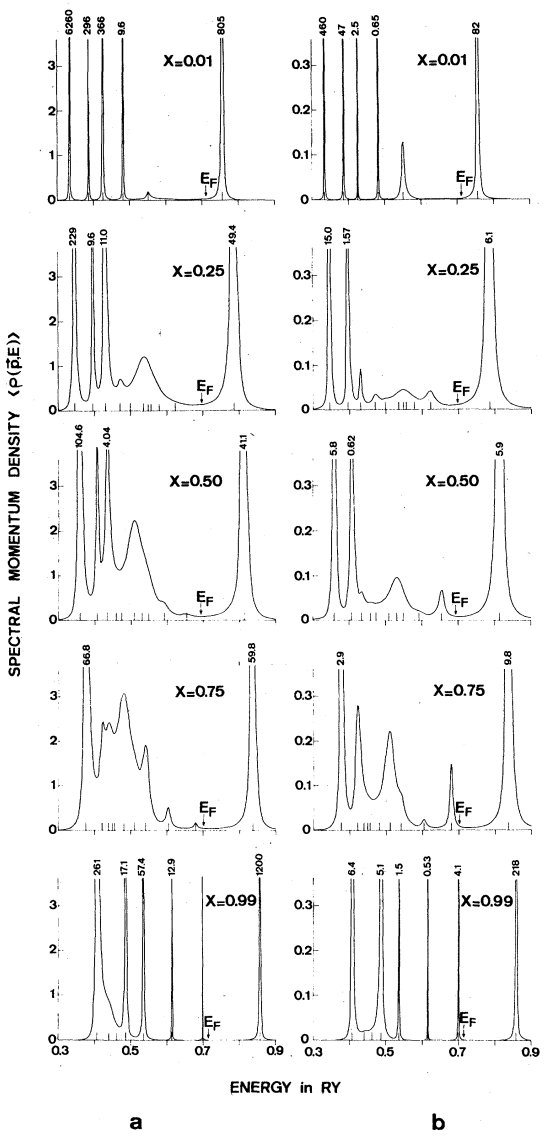

FIG. 1. Spectral momentum density in $Cu_{1-x}Ni_x$ as a function of energy at (a) $\vec{p}=\vec{k}_0\equiv$ (0.166, 0.415, 0.664) $(2\pi/a)$ and (b) $p=\vec{k}_0+\vec{K}_{111}\equiv(1.166,1.415,1.664)$ $(2\pi/a)$, where $a=6.8309$ a.u. is the Cu lattice constant. The real parts of the complex energy solutions of Eq. (3.1) corresponding to $\vec{k}=\vec{k}_0$ are shown as ticks along the horizontal axis for various compositions. Note that the vertical scale on the right-hand set of figures is ten times smaller than for those on the left-hand side.

perfect crystal. However, each of the levels such as $\Gamma_{2'5}$, Γ_{12}, X_2, and X_5 leads to two distinct levels of the same symmetry in the alloy, one of which may be viewed as having its origin in Cu-like d states and the other in Ni-like d states. In this case, the total weights of the two levels in the alloy are roughly proportional to the concentrations $1-x$ and x of Cu and Ni atoms.[10] The preceding discussion of the weights is only meant to be qualitative, and significant deviations from this behavior can arise in specific instances owing to the modulating influence of the factor $\langle t_l(p,\kappa)\rangle/\langle t_l(\kappa,\kappa)\rangle$ in expression (2.2).

Figure 1(a) shows the characteristic changes in the normal contribution to $\langle\rho(\vec{p},E)\rangle$ over the entire range of constituent compositions. For 1 at.% Ni ($x=0.01$), the spectrum is very nearly that of pure Cu, with sharp δ- function-like peaks. Even in this case, however, the peak at 0.55 Ry is strongly damped owing to the nascent Ni impurity level. As more Ni is added ($x=0.25$), a broad structureless impurity peak appears around 0.54 Ry, which with increasing Ni concentration develops into the Ni d bands [see $x=0.5$–0.99 in Fig. 1(a)]. For $x=0.99$, the Ni d bands are seen to yield nearly δ-function-like peaks, except that the lowest energy levels around 0.45 Ry are still strongly perturbed by the Cu-impurity states.

Figure 1(b) shows that the Umklapp contribution to $\langle\rho(\vec{p},E)\rangle$, aside from being an order of magnitude smaller (note scale), generally follows the same trend as a function of Ni concentration as the normal contribution does in Fig. 1(a). As noted above, for a given alloy composition, the structure in $\langle\rho(\vec{k}+\vec{K}_n,E)\rangle$ is controlled by the same complex energy levels at reduced vector $\vec{k}$ for all $\vec{K}_n$. However, differences in the relative weights of the peaks and the overall shape of the $\langle\rho(\vec{p},E)\rangle$ curves in Figs. 1(a) and 1(b), for a fixed x, are expected because $\langle\rho(\vec{k}+\vec{K}_n,E)\rangle$ measures the nth Bloch-like component of the electronic states in the alloy and is therefore different for various reciprocal-lattice vectors $\vec{K}_n$.

Having delineated the nature of the spectral function in the alloy, we discuss the experimentally measurable momentum density $\langle\rho(\vec{p})\rangle$ obtained from $\langle\rho(\vec{p},E)\rangle$ by an integral in energy [cf. Eqs. (2.1) and (2.2)].[32] Figure 2, which compares $\langle\rho(\vec{p})\rangle$ along $\langle 110\rangle$ in $Cu_{0.75}Ni_{0.25}$ with corresponding results in Cu and Ni crystals, shows that the Fermi momentum breaks in the alloy curve are rounded off owing to the damping of the electronic states at the Fermi energy. As the Ni concentration increases, the Fermi momentum breaks move to take into account the shrinking of the Fermi surface, and the $3d$-band contribution in the momentum range between 0.7 and 1.2 a.u. expands. The latter effect is a result of the growth of the Ni $3d$ bands, which possess a charge density that is more concentrated in $\vec{r}$ space (in comparison to Cu) and thus more diffuse in the momentum space.

Figure 3 shows that in $Cu_{0.5}Ni_{0.5}$ the Fermi energy E_F lies above the top of the Ni d bands at the point X in the Brillouin zone. However, by the time the Ni concentration increases to 75 at.%, E_F drops below the X_5 level, leading to the appearance of X-centered hole ellipsoids in the alloy. Note that the crossing of the d bands will not re-

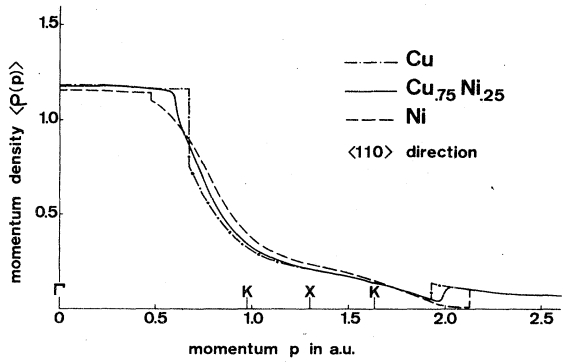

FIG. 2. Momentum density along $\langle 110\rangle$ in $Cu_{0.75}Ni_{0.25}$, Cu, and Ni crystals.

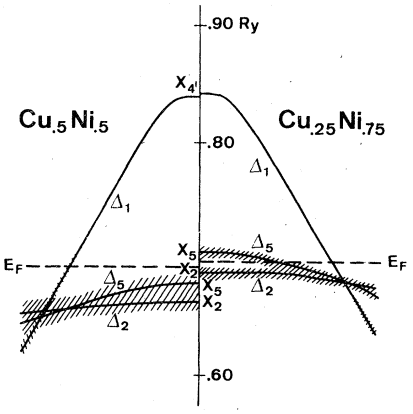

FIG. 3. Complex energy bands near the point X, along the direction $\Gamma\rightarrow X$ in the Brillouin zone in $Cu_{0.5}Ni_{0.5}$ and $Cu_{0.25}Ni_{0.75}$. The vertical length of the shading equals two times the imaginary part of the complex energies.

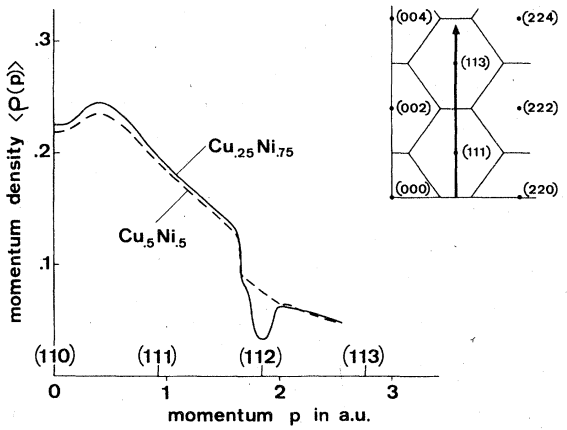

FIG. 4. Momentum density in $Cu_{0.25}Ni_{0.75}$ and $Cu_{0.5}Ni_{0.5}$ along the line joining the reciprocal-lattice points (1, 1, 0) and (1, 1, 3) in momentum space.

sult in a break in the momentum density at the points X in the first Brillouin zone. In fact, due to reasons of symmetry noted above, the momentum density of the entire $\Gamma_{2'5}$-Δ_5-X_5 band is strictly zero in the first zone. The d hole ellipsoids can only be observed in suitably chosen Umklapp contributions. Figure 4 is illustrative in this respect and shows that, compared to $Cu_{0.5}Ni_{0.5}$, the presence of the d hole ellipsoids in $Cu_{0.25}Ni_{0.75}$ yields an extra dip in the momentum density around the momentum vector (1, 1, 2). [The break in $\langle\rho(\vec{p})\rangle$ around 1.6 a.u., which is present in both curves in Fig. 4, is due to the intersection of the Fermi energy with the s-p-like Δ_1 band.] The experimental observation of this dip via Compton scattering or long-slit positron annihilation measurements is unlikely owing to the limited resolution of these methods. Two-dimensional positron annihilation measurements,[21,24,25] however, should be able to see this dip and other similar structures in the momentum density and, thereby, allow us to learn a good deal about the nature of electronic states in disordered alloys.

ACKNOWLEDGMENTS

We are very grateful to Professor S. Berko for several important conservations. The work of A. Bansil was supported in part by the NSF.

APPENDIX A: DETAILS OF Cu AND Ni MUFFIN-TIN POTENTIALS

The Cu and Ni potentials used in the present paper have been used elsewhere in connection with the ATA and CPA electronic spectrum in Cu_xNi_{1-x} and Cu_xZn_{1-x}.[4,5,10] In particular, these potentials are l dependent, and have been obtained by the renormalized-atom technique.[33]

The Cu potential is the same as was used for several density-of-states calculations in the ATA work in Ref. 5 and in all of the more recent CPA work in Ref. 10. This potential was denoted V_{II}^{Cu} in Ref. 5, and differs from another potential V_I^{Cu} which was also used in the earlier CuNi and CuZn ATA work in that the Cu d band in V_{II}^{Cu} is moved to an energy approximately 0.06 Ry higher than in V_I^{Cu}. This was done in Ref. 5 because V_{II}^{Cu} gives better agreement with relevant experimental data pertaining to the placement of Cu d bands with respect to the Fermi energy in crystalline Cu.

Aside from minor differences the Ni potential in the present work is the same as was used in the earlier ATA[5] and some of the CPA work[10] on CuNi. All calculations in the present paper use the fcc lattice structure with a crystalline-Cu lattice constant of 6.8309 a.u. and a muffin-tin zero of −0.834 15 Ry.

APPENDIX B: DERIVATION OF EQUATION (2.9)

The function $R_l(r,E)$ [suppressing the superscripts $A(B)$] satisfies the radial Schrödinger equation

$$R_l''+(2/r)R_l'+[E-V(r)-l(l+1)/r^2]R_l=0. \quad \text{(B1)}$$

The corresponding differential equation for $j_l(pr)$ is

$$j_l''+(2/r)j_l'+[p^2-l(l+1)/r^2]j_l=0. \quad \text{(B2)}$$

It is identical to Eq. (B1) with $E=p^2$ and $V(r)=0$.

Conversion of the form (2.7) for $s_l(p,E)$ into (2.9) involves substitution of $V(r)R_l(r,E)$ from Eq. (B1) into the integrand in Eq. (2.7) and two partial integrations to transfer the derivatives of R_l to $j_l(pr)$, followed by the use of Eq. (B2) to simplify the final expression.

The integral in Eq. (2.7), in contrast to that in Eq. (2.9), involves the potential $V(r)$ in the integrand, which stresses the region near the nucleus where the product of j_l and R_l oscillates rapidly. For this reason, Eq. (2.7) is not as convenient for computational purposes as Eq. (2.9). The manipulations discussed above, in effect, allow us to eliminate $V(r)$ from the integrand in (2.7) and may be useful in evaluating similar integrals in other connections.

[1]R. J. Elliott, J. A. Krumhansl, and P. L. Leath, Rev. Mod. Phys. 46, 465 (1974).
[2]H. Ehrenreich and L. M. Schwartz, in *Advances in Solid State Physics*, edited by H. Ehrenreich, F. Sietz, and D. Turnbull (Academic, New York, 1976), Vol. 31, p. 149.
[3]P. E. Mijnarends and A. Bansil, Phys. Rev. B 13, 2381 (1976).
[4]A. Bansil, H. Ehrenreich, L. Schwartz, and R. E. Watson, Phys. Rev. B 9, 445 (1974).
[5]A. Bansil, L. Schwartz, and H. Ehrenreich, Phys. Rev. B 12, 2893 (1975).
[6]C. D. Gelatt, H. Ehrenreich, and J. A. Weiss, Phys. Rev. B 17, 1940 (1978).
[7]A. Bansil, S. Bessendorf, and L. Schwartz, in *Transition Metals*, Conf. Ser. No. 39, edited by M. J. G. Lee, J. M. Perz, and E. Fawcett (Institute of Physics, Bristol, 1978).
[8]G. M. Stocks, B. L. Gyorffy, E. S. Giuliano, and R. Ruggeri, J. Phys. F 7, 1859 (1977); G. M. Stocks, W. M. Temmerman, and B. L. Gyorffy, Phys. Rev. Lett. 41, 339 (1978).
[9]A. Bansil, Phys. Rev. Lett. 41, 1670 (1978).
[10]A. Bansil, Bull. Am. Phys. Soc. 23, 360 (1978), and (to be published).
[11]P. Chaddah, J. Phys. C 11, 2001 (1978).
[12]K. M. Hong and J. P. Carbotte, Can. J. Phys. 55, 1335 (1977).
[13]P. T. Coleridge and I. M. Templeton, Can. J. Phys. 49, 2449 (1971).
[14]R. Griessen, W. J. Venema, J. K. Jacobs, F. D. Manchester, and Y. de Ribaupierre, J. Phys. F 7, L133 (1977).
[15]R. J. Nastasi-Andrews and R. E. Hummel, Phys. Rev. B 16, 4314 (1977).
[16]K. Y. Yu, C. R. Helms, W. E. Spicer, and P. W. Chye, Phys. Rev. B 15, 1629 (1977); P. Heimann, H. Neddermeyer, and M. Pessa, Phys. Rev. B 17, 427 (1978).
[17]For a review of the experimental aspects see D. J. Sellmeyer, in *Advances in Solid State Physics*, edited by H. Ehrenreich, F. Seitz, and D. Turnbull (Academic, New York, 1978), Vol. 33.
[18]W. Gudat and C. Kunz, Phys. Status Solidi B 52, 433 (1972).
[19]*Compton Scattering*, edited by B. Williams (McGraw-Hill, London, 1977).
[20]R. N. West, Adv. Phys. 22, 263 (1973).
[21]S. Berko and J. Mader, Appl. Phys. 5, 287 (1975).
[22]P. E. Mijnarends, in *Positrons in Solids*, edited by P. Hautojärvi (Springer, Berlin, to be published).
[23]On the other hand, the repulsion of the positrons by the nucleus has the advantage of deemphasizing the uninteresting contribution from the closed-shell core electrons to the annihilation profile. In Compton scattering these core electrons contribute fully and, especially in high-Z materials, tend to mask the effects of alloying on the valence electrons.
[24]S. Berko, M. Haghgooie, and J. J. Mader, Phys. Lett. A 63, 335 (1977).
[25]R. J. Douglas and A. T. Stewart, Paper H14, Fourth International Conference on Positron Annihilation, Helsingør, 1976 (unpublished).
[26]S. Berko in *Positron Annihilation*, edited by A. T. Stewart and L. O. Roellig (Academic, New York, 1967), pp. 61–79.
[27]S. Berko and A. P. Mills, J. Phys. (Paris) 32, C1-287 (1971).
[28]P. E. Mijnarends, Physica (Utrecht) 63, 248 (1973).
[29]R. Harthoorn and P. E. Mijnarends, J. Phy. F 8, 1147 (1978).
[30]It is in this sense that the momentum density, even in a disordered alloy, can be viewed as being built out of contributions from some sort of individual $\vec{k}$ states. This correspondence with a perfect crystal, however, is an artifact of the theory. Physically, there are no perfect Bloch states in a disordered alloy, and the spectral momentum density $\langle\rho(\vec{p}, E)\rangle$ consists of peaks of finite width as a function of E for fixed $\vec{p}$, and also as a function $|\vec{p}|$ for a given E.
[31]These symmetry considerations do not apply to the spectral density function $\langle\tilde{A}(\vec{k}, E)\rangle$ which enters the computation of the average density of states. As discussed in Ref. 3, $\langle\tilde{A}(\vec{k}, E)\rangle = \sum_{\vec{K}_n}\langle\rho(\vec{k}+\vec{K}_n, E)\rangle$, and therefore this function involves contributions from all momenta $\vec{p}=\vec{k}+\vec{K}_n$.
[32]The Compton and positron annihilation experiments measure integrals of $\langle\rho(\vec{p})\rangle$ over planes or, in the latter case, along lines in momentum space. The three-dimensional momentum density is obtainable only by a suitable inversion of the experimental data; see, e.g., P. E. Mijnarends, in *Compton Scattering*, edited by B. Williams (McGraw-Hill, London, 1977), Chap. 10.
[33]L. Hodges, R. E. Watson, and H. Ehrenreich, Phys. Rev. B 5, 3953 (1972).